Site-Dependent Properties of Quantum Emitters in Nanostructured Silicon Carbide

Tamanna Joshi and Pratibha Dev*
Department of Physics and Astronomy, Howard University, Washington, DC 20059, USA

(Received 13 September 2021; revised 2 February 2022; accepted 4 April 2022; published 5 May 2022)

Deep defects in silicon carbide (SiC) possess atomlike electronic, spin, and optical properties, making them ideal for quantum computing and sensing applications. In these applications, deep defects are often placed within fabricated nanostructures that modify defect properties due to surface and quantum confinement effects. Thus far, theoretical studies exploring deep defects in SiC have ignored these effects. Using density-functional theory, this work demonstrates site dependence of properties of bright negatively charged silicon monovacancies within a SiC nanowire. It is shown that the optical properties of defects depend strongly on the hybridization of the defect states with the surface states and on the structural changes allowed by proximity to the surfaces. Additionally, analysis of the first-principles results indicates that the charge-state conversion and/or migration to thermodynamically favorable undercoordinated surface sites can deteriorate deep-defect properties. These results illustrate the importance of considering how finite-size effects tune defect properties and of creating mitigating protocols to ensure the charge-state stability of a defect within nanostructured hosts.

DOI: 10.1103/PRXQuantum.3.020325

I. INTRODUCTION

Silicon carbide (SiC) hosts a number of bright deep defects that are promising for use as quantum bits (qubits) in quantum information [1–6], and quantum-enhanced sensing applications [7]. The quantum emitters in SiC have addressable spins [8–10], long spin coherence times [9,11], and near-telecom-range quantum emissions [11,12]. But, above all, what gives SiC an edge over other wide-band-gap hosts such as diamond is that it is an industrially mature material, allowing for nanofabrication and scalability. It also exists in a number of low-energy cubic (3C-SiC) and hexagonal (2H-, 4H-, and 6H-SiC) polytypes, providing a practical and large playing field for the implementation of different technologies.

Notwithstanding the progress made in the field, the exploration of SiC as a host to quantum emitters is a relatively new endeavor [13] and there are still challenges in integrating quantum emitters in SiC into photonics and in optimizing the generation of the deep defects within SiC [14]. In addition, very few experiments [15,16] and no theoretical studies (to the best of our knowledge), which are usually performed in bulk SiC, have probed surface and/or finite-size effects, even though shallower defects are desirable for sensing applications. These effects also become important when the quantum emitters are placed in optical nanophotonic cavities [17–21], nanoscale solid immersion lenses [22], and arrays of nanopillars [4,5,23]. In such nanofabricated devices, there will inevitably be defects close to surfaces or sidewalls. This can change, or even deteriorate, the optical properties of a defect and make the bright (photoluminescent) charge state unstable as different finite-size effects come into play within a nanostructure [5,24,25]. In the present work, we investigate the effects of nanostructuring on structural, electronic, spin, and optical properties of defects using density-functional theory (DFT). In particular, we show how quantum confinement and surface effects influence the properties of the bright negatively charged silicon vacancy (V_{Si}^{-1}) by placing these defects in a 2H-SiC nanowire (NW). We choose V_{Si}^{-1} as our proof-of-principle defect because it is a particularly noteworthy qubit candidate; it shows an optically accessible high spin state ($S = 3/2$) [2,26], a high emission into the zero-phonon line (ZPL) [4], spectral stability [27,28], and long room-temperature spin coherence [2,10,22]. Our results demonstrate that the deterioration of the optical signal from the bright monovacancies close to the surfaces can be attributed to conversion to a dark charge state and/or defect migration to the thermodynamically favorable undercoordinated surface sites, which act as a sink to the defects. These results illustrate the importance

*pratibha.dev@howard.edu

Published by the American Physical Society under the terms of the Creative Commons Attribution 4.0 International license. Further distribution of this work must maintain attribution to the author(s) and the published article's title, journal citation, and DOI.

of: (i) considering how finite-size effects can change and, hence, be leveraged to tune the properties of defects by deterministic placement of the defects at different distance from the surfaces via use of different implantation techniques [29,30]; and (ii) creating mitigating protocols to ensure the charge-state stability of a defect within nanostructured hosts via different surface passivation schemes.

II. COMPUTATIONAL DETAILS

All of the first-principles DFT-based calculations use the generalized gradient approximation (GGA) [31] of Perdew, Burke, and Ernzerhof [32], implemented within the QUANTUM ESPRESSO software package [33,34]. As we use ultrasoft pseudopotentials, we find that cutoffs of 40 Ry and 350 Ry are sufficient for expanding the wave functions and charge densities. All structures are fully relaxed until the forces on the atoms are below 10^{-3} Ry/a.u.

In this work, we choose the 2H-SiC polytype (over the 4H- and 6H-SiC polytypes) as it allows us to create a nonmagnetic nanostructure. Nevertheless, our qualitative results are general and should apply to other choices of SiC polytypes as well, even if finer quantitative details may differ due to the different stacking sequences of the tetrahedrally bonded silicon and carbon atoms along the c axis. The 2H-SiC NW, shown in Fig. 1(a), is periodic in the [0001] direction and consists of 216 atoms. It is about 15.43 Å in diameter. Periodic images of the NW in the lateral directions are separated by a vacuum of about 12 Å. Brillouin-zone sampling is carried out by using a Γ-centered k-point grid of $1 \times 1 \times 6$ according to the Monkhorst-Pack scheme [35]. The as-created pristine NW is stoichiometric and nonmagnetic. This can be seen in Fig. 1(b), which shows the spin-resolved density of states (DOS) with completely symmetric contributions from the two spin channels. The absence of magnetic defects in the pristine NW ensures that once silicon vacancies are introduced, there are no additional interactions between the spins of silicon vacancies and those of magnetic surface defects. Although, in experiments, there can be other magnetic defects in the interior and on the surface of such a nanostructure, our choice of a nonmagnetic pristine nanowire allows us to concentrate on the role of finite-size effects by themselves in changing the properties of deep-level defects, once the latter are introduced.

In the equilibrium structure of the pristine NW, there are three distinct NW sites at which we create a silicon vacancy [see Figs. 1(a) and 1(c)]: (i) fourfold-coordinated Si atoms in the interior of the NW (S1), (ii) fourfold-coordinated Si atoms on the NW surface (S2), and (iii) threefold site on the surface (S3). Since the defects can undergo charge conversion from the bright (i.e., photoluminescent) negatively charged state to the dark neutral state upon photoexcitation, we study the properties of V_{Si} in both of these charged states. The formation energy,

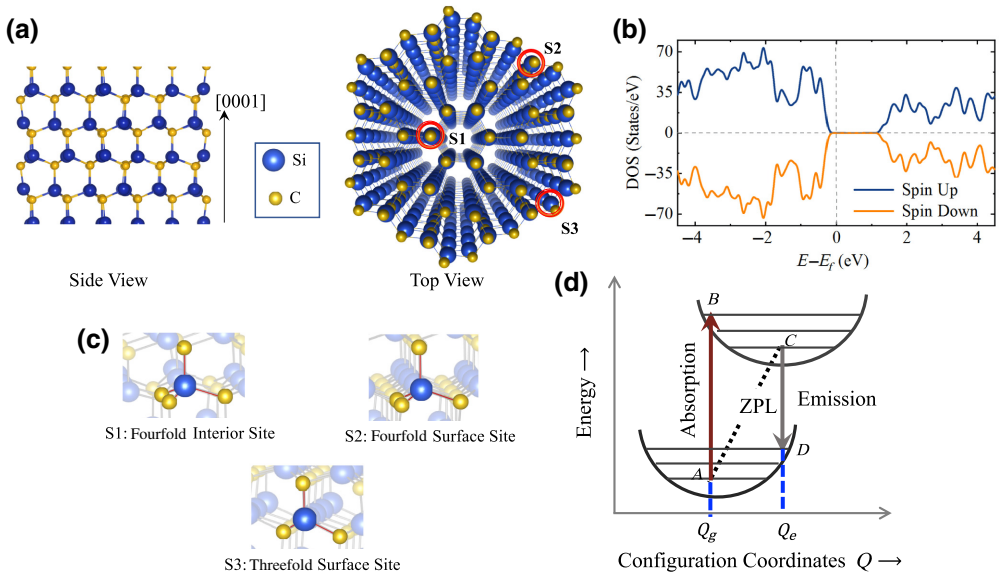

FIG. 1. The 2H-SiC nanowire. (a) Side and top views of pristine and/or defect-free NW, periodic along the [0001] direction. (b) The spin-resolved density-of-states (DOS) plot for the pristine NW, showing that it is nonmagnetic. (c) The three distinct silicon sites [circled in (a)] at which the defects are created: the tetrahedrally bonded interior site (S1), the fourfold-coordinated surface site (S2), and the undercoordinated site on the surface, bonded to only three carbon atoms (S3). (d) The configuration coordinate diagram, giving the total energy as a function of the ground- (bottom) and excited-state (top) configurations within the Franck-Condon picture. It is used to emulate the photoexcitation process, which is calculated using the constrained-occupation DFT (CDFT) method.

ΔE^{form}, of the defect X in charged state q is defined as

$$\Delta E^{\text{form}}[X^q] = E_t[X^q] - E_t[P] - \sum_i n_i \mu_i + q\,(E_v + E_F + \Delta V)\,, \quad (1)$$

where $E_t[X^q]$ is the total energy of the defective system, $E_t[P]$ is the total energy of the pristine and/or defect-free system, q is the charged state of the defect, E_v is the valence-band maximum, E_F is the Fermi energy referenced to the valence-band maximum, ΔV is the potential alignment term, μ_i is the chemical potential of the i^{th} atom, and the integer n_i represents the number of atoms added (positive integer) or removed (negative integer).

Since 2H-SiC is a lesser-studied polytype as compared to other hexagonal polytypes, we also determine the properties of monovacancies in the bulk in order to highlight the effects of nanostructuring. The bulk calculations are carried out on an $8 \times 8 \times 2$ supercell, consisting of 512 atoms. The size of the bulk supercell ensures that the distances of the defects from their periodic images in the lateral and vertical directions are the same or similar for the NW and the bulk supercell. Even though the bulk supercell is large, we use a Γ-centered $2 \times 2 \times 6$ k-grid. In our previous works on negatively charged silicon vacancies in a bulk 4H-SiC supercell of a similar size [2,3,26], we have found that a finite-size k-grid is necessary to accurately describe the defect properties and that using only a Γ-point calculation may lead to erroneous results.

In order to study the effect of nanostructuring on the excited state properties, we calculate the ZPL for V_{Si}^{-1} in the NW and in the bulk using the constrained-occupation DFT (CDFT) method [see Fig. 1(d)]. CDFT has been shown to be a suitable and computationally inexpensive method for calculating ZPL energies for deep defects with excitations between highly localized (nearly dispersionless) defect states, where the excited state can also be represented by a single Slater determinant [36,37]. Within the CDFT method, the spin-preserving photoluminescence process is emulated by constraining the occupation of the defect states in the optically active spin channel. The CDFT results are then mapped onto the Franck-Condon picture, giving optical transition energies. In this picture, the vertical transitions from A to B and C to D in Fig. 1(d) correspond to the photon absorption (excitation) and emission (deexcitation) processes, respectively. The difference between the total energies of the relaxed structures in the excited state (point C) and the ground state (point A) correspond to the ZPL energy. The Stokes shift is calculated by finding the difference in the vertical excitation (absorption) and the ZPL.

III. RESULTS

A. Negatively charged silicon vacancy in bulk

In the bulk 2H-SiC, a V_{Si}^{-1} leaves a total of five electrons in four sp^3-hybridized dangling bonds on the surrounding carbon atoms. The resulting equilibrium structure has a C_{3v}-point group symmetry as seen in Fig. 2(a) [only nearest-neighbor (NN) carbons are shown for clarity]. It should be pointed out that the defective structure has only weakly broken T_d symmetry, with the distances from the defect site to the three equivalent carbon atoms in the basal plane and to the carbon on the C_3 axis (along the crystalline [0001] direction) differing by a mere 0.8×10^{-2} Å. Our calculations show that in the bulk crystal, V_{Si}^{-1} is a spin-3/2 defect, consistent with the experimental and theoretical results obtained for other polytypes of SiC [2,3,26]. Figure 2(b) is an isosurface plot of the spin density ($\Delta\rho = \rho^{\uparrow} - \rho^{\downarrow}$, ρ = charge density) for V_{Si}^{-1}, showing that the defect-induced spins are mostly localized on the four NN carbons. This is due to the highly localized nature of the $2s$ and $2p$ orbitals that form the dangling bonds on the carbons surrounding the defects. The large exchange interactions between the spatially localized unpaired electrons in the defect states leads to the observed spin-polarized structures, which is also seen in deep defects involving the $2s$- and $2p$-derived defect states of other second-row elements [37–40]. This means that there are more electrons in the majority-spin channel (spin up) than in the minority-spin channel (spin down). In order to further understand the electronic, spin, and optical properties of V_{Si}^{-1}, we form single-electron molecular orbitals (MOs) for the defect states. The MOs are created from the symmetry-adapted linear combinations of three equivalent dangling sigma bonds (σ_1, σ_2, and σ_3) from the carbon atoms in the basal plane and the orbital, σ_4, belonging to the carbon atom on the C_3 axis. These symmetry-adapted MOs include two singlet states, $a_1 = c_1(\sigma_1 + \sigma_2 + \sigma_3) + c_2\sigma_4$ and $\tilde{a}_1 = \tilde{c}_1(\sigma_1 + \sigma_2 + \sigma_3) + \tilde{c}_2\sigma_4$, and the doubly degenerate states, $e = \{e_X = c_3(2\sigma_3 - \sigma_1 - \sigma_2),\ e_Y = c_4(\sigma_1 - \sigma_2)\}$. Here, we label the defect states by their symmetry and the coefficients [$c_i/\tilde{c}_i$] ensure that the MOs are normalized. The "tilde" on the molecular orbital, $\tilde{a}_1$, is placed to distinguish it from the other defect state also belonging to the a_1 representation. The energy ordering of these states can be obtained from the DFT calculations. Figure 2(c) plots the energy-ordered defect states (optically active minority spin channel only) in the ground state. This ordering of the defect states implies that the ground state has the following electronic configuration: $a_1^{\uparrow\downarrow}\tilde{a}_1^{\uparrow}e^{\uparrow\uparrow}$. As the structure has only a weakly broken T_d symmetry, the doubly degenerate e states are only about 1.18×10^{-2} eV above the $\tilde{a}_1$ states. This means that the spin-preserving optical excitations from the ground state to the two possible excited states will have very similar energies. Figure 2(d) is a schematic diagram (not to scale), showing (from left to

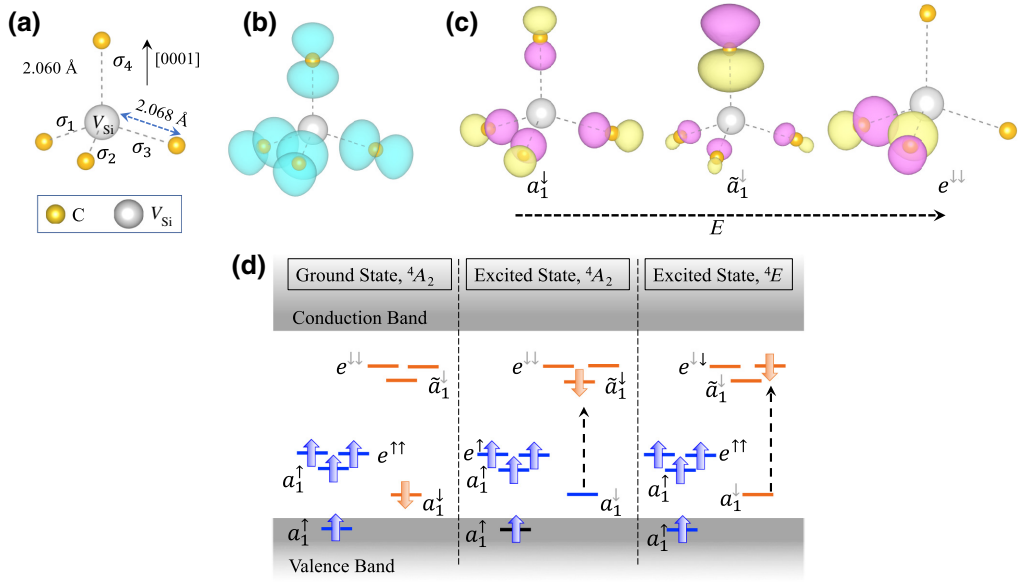

FIG. 2. A charged silicon monovacancy in bulk 2H-SiC. (a) The C_{3v}-point group symmetry of V_{Si}^{-1}. Only the nearest-neighbor (NN) carbon atoms are shown for clarity. (b) The spin-density (difference in charge densities within the two spin channels) isosurface plot (in blue), showing the spatially localized nature of the defect-induced spins. (c) Charge-density plots for the optically active defect states (minority spin) that are involved in the photoexcitation process. From left to right, the lowest-energy filled singlet state (a_1 symmetry), an unoccupied singlet, $\tilde{a}_1$, and one of the doubly degenerate unoccupied e states. The pink (yellow) color corresponds to positive (negative) isovalues. The defect states are labeled by their respective group-theoretic representations. The black (gray) arrows in the superscripts of the labels are used to emphasize that the states are filled (empty). (d) A schematic single-particle-level diagram (not to scale), showing the defect states introduced by V_{Si}^{-1} in the ground state and the two excited states.

right) the electronic configurations in the ground state ($^4A_2$ symmetry) and the two possible excited states with $^4A_2$ symmetry and ^4E symmetry. We use capital letters for the group-theoretic representations of the many-body ground and excited states. The lowest-energy optical excitation is from the ground state, $^4A_2$ $[a_1^{\uparrow\downarrow}\tilde{a}_1^{\uparrow}e^{\uparrow\uparrow}]$ to the excited $^4A_2$ state $[a_1^{\uparrow}\tilde{a}_1^{\uparrow\downarrow}e^{\uparrow\uparrow}]$. For this excitation, the ZPL energy is calculated to be 1.19 eV. Our results presented thus far for the ground- and excited-state properties of V_{Si}^{-1} in the bulk 2H-SiC are consistent with those obtained for other polytypes of SiC [26]. It is expected that the nanostructuring of the host crystal will modify the bulk properties. These modifications are critical to understanding experiments on nanostructured SiC.

B. Negatively charged silicon vacancy in the NW

The equilibrium structure of the pristine NW [Fig. 1(a)] shows the characteristic contraction of bonds between atoms on the surface of the nanowire [41]. This contraction is mostly driven by the surface effects, since the chemical environment of the atoms on the surface is different from that of the underlying bulk. This results in a coordination-dependent reconstruction of bonds on the NW surface. For the undercoordinated surface sites, the three remaining bonds are strengthened, with the average basal plane bonds contracting by about 3.20% and the bond along the axial direction showing a contraction of about 8.50%. The fourfold-coordinated surface sites show a much smaller contraction, where the bond lengths change to accommodate structural changes imposed by the neighboring threefold-coordinated sites, with which they share atoms. For these sites, the bond lengths for atoms on the basal plane contract by about 0.65% and the bond along the axial direction contracts by about 0.50%. Moving inward toward the NW center, different sites show changes in bond lengths to accommodate structural changes at the surface. For example, the fourfold interior site used in the present study shows a slight increase in bond lengths—about 0.15% and 0.76% increases in the axial and basal directions, respectively. The tendency of the nanostructures to reduce surface energy via skin-bond contraction is expected to affect different defect properties.

The site-dependent spins, spin polarization energies, and defect-formation energies of V_{Si}^{-1} in the SiC NW are plotted in Fig. 3(a). Properties of defects in the bulk are provided for comparison, where appropriate. The net spin remains 3/2 at a site in the NW interior and the fourfold-coordinated site on the surface of the NW, which is consistent with the bulk calculations. On the other hand, V_{Si}^{-1} at the undercoordinated site is a spin-1/2 defect. Site dependence is also observed in the spin polarization energy, which is defined as the energy difference between the magnetic and

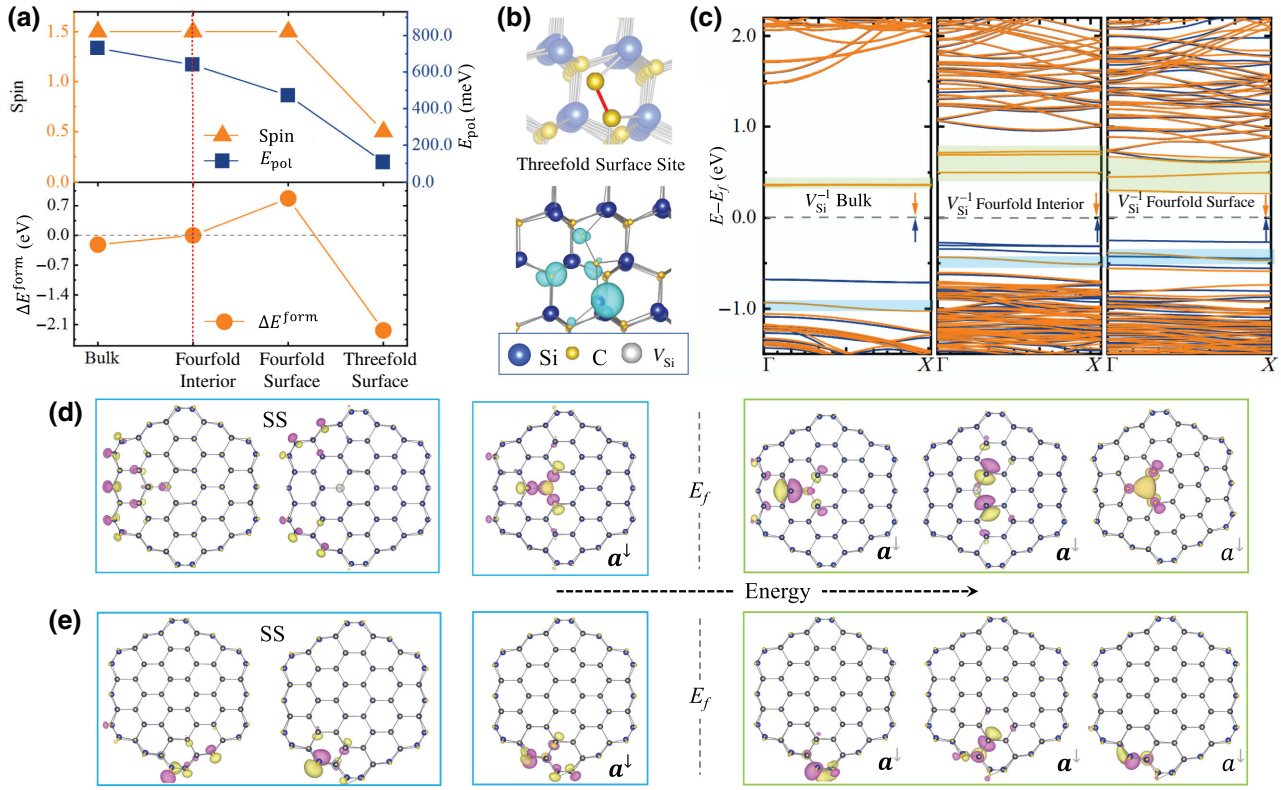

FIG. 3. A negatively charged silicon vacancy, V_{Si}^{-1}. (a) The site-dependent spin, spin polarization energy ($E_{pol} = E_{nonmagnetic} - E_{magnetic}$), and formation energy, ΔE^{form}, of the defects at different sites in the NW. The defect-formation energy at the interior of the wire is used as the reference. (b) The equilibrium geometry for V_{Si}^{-1} at the threefold-coordinated surface site, showing dimerization of carbon atoms. The lower figure is a plot of the spin-density difference (in blue), showing the distribution of the spin of the defect on atoms around V_{Si}^{-1}. (c) Band structures (from left to right) for V_{Si}^{-1} created in bulk 2H-SiC, at the NW center, and the fourfold-coordinated site at the NW surface, respectively. The optically active (spin-down channel) defect states are highlighted. The Fermi energy, E_f , is used as the reference. Charge-density plots for the optically active defect states (energy ordered) for the defect at (d) the NW center and (e) the fourfold-coordinated site on the NW surface. Also shown are donorlike surface states (SSs) that are just below the filled defect states and that show a hybrid defect-surface-state character. The pink (yellow) color corresponds to positive (negative) isovalues.

nonmagnetic structures ($E_{pol} = E_{nonmagnetic} - E_{magnetic}$). For all sites, the calculated values of E_{pol} are substantially larger than the room-temperature thermal energy ($k_B T \approx$ 25 meV), showing that the spins in not only the bulk but also in the NW will survive well beyond room temperature. The defect-formation energies at different sites in Fig. 3(a) are given using the formation energy in the center of the NW as the reference. As expected, the formation energies in the bulk and the interior of the NW are comparable. On the other hand, the formation energy at the fourfold-coordinated surface site on the surface is higher than that in the interior of the NW, even though the creation of the silicon vacancy requires breaking four covalent bonds for both sites. This can be traced back to the contraction of the bonds on the surface of the NW, with a concomitant increase in bond strengths on the surface. For the threefold-coordinated site, we find that the formation energy is substantially smaller (by approximately 2.23 eV) as compared to the defect in the center of the NW [see Fig. 3(a)]. The decrease in the defect-formation energy at the undercoordinated site can be attributed to: (i) having to break only three strong covalent bonds at a threefold site, as compared to any other site where the silicon is tetrahedrally bonded to carbon atoms; and (ii) large reconstruction at the undercoordinated site, once V_{Si}^{-1} is created. Figure 3(b) shows this reconstruction at the defect site, with two of the three carbons around the defect dimerizing and forming a chemical bond with each other, thereby reducing the energy of the structure considerably. The bonding of the carbon atoms at the defect site also reduces the net spin of V_{Si}^{-1} to a value of 1/2 instead of the expected spin-3/2 value obtained for the defects in fourfold-coordinated sites in the bulk and NW. The spin-density difference plotted in Fig. 3(b) shows that the 1/2 spin of this defect is distributed on different atoms around the defect, with large contributions coming from nearby

Si- and C atoms. Hence, V_{Si}^{-1} at the threefold site loses its desirable electronic and spin properties (see Fig. 1 in the Supplemental Material [42]) and is no longer usable as a spin-3/2 qubit.

Figure 3(c) shows the band structures (from left to right) for the V_{Si}^{-1} defect created in the bulk 2H-SiC, at the NW center, and the fourfold-coordinated site at the NW surface. The nearly dispersionless defect states belonging to the optically active spin-down channel are highlighted. Unlike bulk 2H-SiC, where the $\tilde{a}_1$ and e states are almost degenerate, there is a complete loss of degeneracy of the unoccupied defect states in the NW, as can be seen in Fig. 3(c). This is due to the much lower symmetry (C_1) of the V_{Si}^{-1} defects in the NW. Thus, for V_{Si}^{-1} at the fourfold-coordinated sites, there can be several possible spin-preserving and dipole-allowed optical excitations between the defect states. In the case of the fourfold-coordinated interior site, we find that there are three possible excitations from the filled spin-down singlet state to the three empty defect states. The charge-density isosurfaces of each of these states involved in the excitations are shown in Fig. 3(d), where the pink and yellow colors correspond to the positive and negative isovalues, respectively. The lowest-energy photoexcitation involves the highest filled spin-down defect state (belonging to the a representation) to the lowest empty spin-down singlet state, which also has a symmetry. The corresponding ZPL is calculated to be 0.87 eV, which is much lower than the ZPL in the bulk. In addition to the in-gap filled defect state, there are two nearly degenerate filled states (spin-down channel) that lie about 0.17 eV below the highest filled defect state. These donor states are mostly localized on the surface, though one of them shows some defect-state character. The surface states (SSs) may participate in the photoexcitation process. Figure 2 in the Supplemental Material [42] shows these in-gap states (surface and defect states) for a smaller isovalue, further highlighting their nature and the extent of hybridization between the defect states and the surface states.

In the case of the fourfold-coordinated surface site, we find three filled spin-down (optically active spin channel) in-gap states, which are spatially localized. They show a hybrid defect-surface character, with carbon atoms surrounding the defect, as well as the adjacent surface atoms, contributing to these states [see Fig. 3(e)]. The two lower in-gap states lie below the highest filled state by about 0.44 eV and 0.16 eV. All three of the in-gap states may participate in the photoexcitation process. The ZPL energy for the lowest-energy optical excitation, involving the highest filled spin-down singlet defect state to the lowest empty spin-down singlet state, is calculated to be 0.70 eV, which is smaller than the ZPL values calculated in the bulk and interior of the NW. We also find that highest empty spin-down defect state is resonant with the surface states close to the conduction-band edge. Electrons excited to these surface states via off-resonant excitations or via two photon processes may lead to either blinking, if the surface states act as the shelving state [43], and/or photobleaching of the defect with a permanent loss of electron upon excitation. Hence, we find that upon photoexcitation, there are a number of processes that can result in a change from the bright to dark charge state [44] of the defect, converting V_{Si}^{-1} to V_{Si}^{0}. As the latter has unknown photoluminescence properties and its electronic structure properties have remained somewhat controversial [45–47], we present its electronic and spin properties in Note I and Fig. 3 in the Supplemental Material [42]. Our results show that the defect in bulk SiC prefers to be in a high spin state ($S = 1$), in agreement with Zywietz *et al.* [45] and Torpo *et al.* [46].

IV. DISCUSSION

The potential loss of signal from the V_{Si}^{-1} defects close to the surfaces of the nanostructured host will be deleterious to the performance of devices based on these defects and requires further understanding so that mitigating protocols can be designed. Our calculated band structures for the monovacancies in the NW [Fig. 3(c)] show the presence of donor-type and acceptor-type surface states, which are close to the defect states in energies. In addition, due to the proximity of the V_{Si}^{-1} defects considered here to the surfaces, the defect states show some hybridization with the surface states. As a consequence, these surface states may become involved in the photoexcitation processes in several ways, which may lead to temporary or permanent loss of the charge from the defect. Examples of different photoexcitation processes that may lead to luminescence and/or charge conversion to a dark state are illustrated in Figs. 4(a)–4(c). Figure 4(a) is a schematic diagram showing the processes of photoexcitation [$V_{Si}^{-1} \rightarrow (V_{Si}^{-1})^*$] and deexcitation [$(V_{Si}^{-1})^* \rightarrow V_{Si}^{-1}$], resulting in photoluminescence from the V_{Si}^{-1} defect in the NW. Here, $(V_{Si}^{-1})^*$ refers to a photoexcited defect. The levels are not drawn to scale and thus apply to all fourfold-coordinated sites in the NW considered here. Also, both the donor-type and acceptor-type surface states localized on the surfaces are shown as thin colored bands. Figure 4(b) shows a two-photon absorption process [ⓘ followed by ⓘⓘ]. The electron can then be temporarily trapped by the surface states, which may act as shelving states [43], and then undergo phosphorescence [marked as ⓘⓘⓘ], resulting in blinking. Alternatively, the electron can migrate away from the defect, resulting in a $V_{Si}^{-1} \rightarrow V_{Si}^{0}$ charge conversion, with the latter being a dark charge state. Figure 4(c) shows another pathway for charge conversion to a neutral state, involving a two-photon absorption process [steps ⓘ and ⓘⓘ] followed by an Auger process in which energy released in step ⓘⓘⓘ is used to ionize an electron away from the defect in step ⓘⓥ [48]. Hence, the photoexcitation process itself can result in

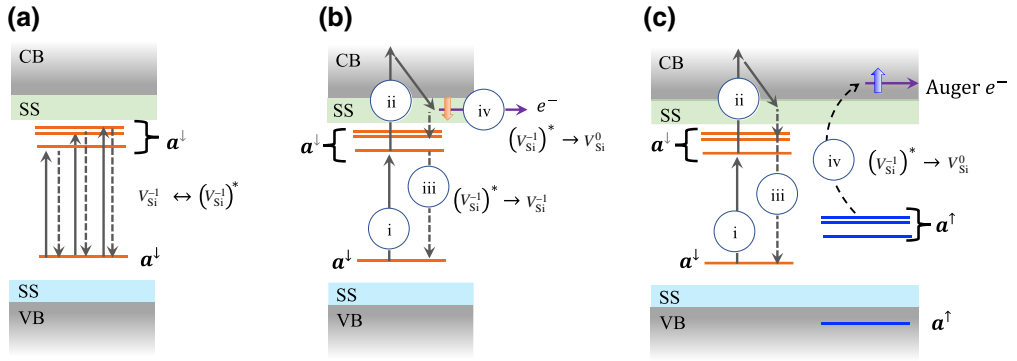

FIG. 4. The optical excitation and charge conversion of V_{Si}^{-1}. (a) A schematic diagram (not to scale) showing the photoexcitation [$V_{Si}^{-1} \rightarrow (V_{Si}^{-1})^{*}$] and deexcitation [$(V_{Si}^{-1})^{*} \rightarrow V_{Si}^{-1}$], resulting in photoluminescence from the V_{Si}^{-1} defect in the NW. Only the filled and empty minority-spin defect states (all belonging to the a representation) are shown. $(V_{Si}^{-1})^{*}$ refers to the excited state of the defect. The donor- and acceptor-type surface states (SSs) are indicated. (b) A schematic diagram showing the excitation of an excited defect [i.e., ⓘ; followed by ⓘⓘ] in a two-photon absorption process. Scattered into the localized acceptorlike surface state, the electron can either undergo phosphorescence [marked as ⓘⓘⓘ], resulting in blinking, or it can migrate away from the defect, resulting in a $V_{Si}^{-1} \rightarrow V_{Si}^{0}$ charge conversion, with the latter being a dark state. (c) A schematic diagram showing another possible route to charge conversion to the neutral state, involving a two-photon absorption process [ⓘ followed by ⓘⓘ] followed by an Auger process [marked by ⓘⓘⓘ and ⓘⓥ] that ionizes the defect. Here, the filled majority spin states are also shown because the spin-up electron is ionized from the defect. VB and CB stands for valence and conduction bands, respectively.

signal deterioration, with a temporary or permanent loss of an electron from the photoexcited defect. Our calculations also reveal a second potential source for the loss of signal from a defect close to the NW surface. As discussed earlier, the defect-formation energies at the undercoordinated surface sites are much lower than at any other site in the NW. Hence, the defect itself can migrate to the thermodynamically favorable undercoordinated surface sites, where the defects have very different structural, electronic, and spin properties.

We would also like to note that V_{Si}^{-1} has a stable spin state at different fourfold-coordinated sites within the NW, irrespective of the local strain at the sites. There is, however, a site-dependent shift in the ZPL for the lowest-energy excitation of the V_{Si}^{-1} in the NW as compared to the bulk. The calculated values of ZPL for the fourfold sites in the interior and on the surface of the NW are about 325.6 meV and 491.1 meV lower than the bulk value, respectively. The lowering of the ZPL value at the fourfold sites in the NW can be attributed to several mutually dependent effects, including: (i) local strain due to the skin-contraction effect, (ii) large structural changes in the NW upon photoexcitation, (iii) the hybridization between the surface states and the defect states, and (iv) a lowering of symmetry compared to bulk, which splits the unoccupied defect states, reducing the gap between the frontier orbitals (i.e., the highest occupied and lowest unoccupied defect states) involved in the lowest-energy photoexcitation. The relative importance of these four factors can be gauged from the DFT results. Estimating the strains by the changes in the bond lengths at the respective sites and using the experimentally deduced value of the strain-coupling parameter of 1130 meV $(\text{strain})^{-1}$ (in the basal direction) [16], we can obtain an order-of-magnitude estimate of the ZPL shift due to strain. We find that at all fourfold sites in the NW, the strain-induced changes in the ZPL (as compared to the bulk) are about 10 meV or less. Although our calculated strain-dependent changes in the ZPL agree with the experimentally observed shifts [16], they are 2 orders of magnitude smaller than the total ZPL changes calculated for the fourfold-coordinated sites within the NW. This means that the local strain is not the leading cause of the changes in the ZPL for different sites in our NW. This conclusion is different from that reached by Vásquez *et al.* [16], where the authors surmise that the strain is the leading cause of the ZPL shift in their experimental study of strain-effects within SiC nanostructures. We would like to emphasize that these different conclusions do not necessarily mean that there is a contradiction. It is most likely that the difference in conclusions reached in our theoretical work and the experiment is due to the large sizes (a few hundreds of nanometers to a few micrometers) of their nanoparticles, with defects that are located much farther away from the surfaces of their nanoparticles than in our study. In turn, this will have minimized the importance of other surface effects in experiment that play a prominent role in our study. In order to quantify the effect of the second factor—structural changes upon photoexcitation—we calculate the Stokes shift, which is given by the difference in the vertical excitation and the ZPL. We find that the Stokes-shift values are about 104.9 meV, 138.6 meV, and 169.7 meV in the bulk, at the site in the NW interior, and

at the fourfold site on the NW surface, respectively. In turn, this means that the monovacancies in the NW undergo larger structural changes upon photoexcitation. However, the ZPL shift attributable to the changes in Stokes shift in the NW as compared to the bulk is still an order of magnitude smaller. The third factor that causes ZPL shift is the hybridization between defect states and the surface states of the NW. This is especially pronounced in the defect at the surface. On one hand, there is a hybridization between the donorlike localized surface states and the filled defect states, forming bonding and antibonding MOs. The antibonding MOs, which are mostly defect state in character, are pushed up within the band gap. On the other hand, the empty defect states, which hybridize with the acceptorlike surface states, are pushed down in energy. This reduction in the gap between filled and empty defect states would then lead to the ZPL shift. Lastly, the lowering of symmetry itself at different fourfold-coordinated sites in the NW as compared to the bulk splits what are nearly degenerate empty defect states. As a result, there is a further reduction in the gap between the frontier orbitals. The influence of the last two factors can be seen in the energy splitting between the frontier orbitals, which we calculate to be about 1287.7 meV, 938.3 meV, and 833.3 meV for the V_{Si}^{-1} in bulk, at the NW interior site, and at the NW surface site, respectively. Hence, we find that the energy-gap reduction in the frontier orbitals of V_{Si}^{-1} in the NW interior and the NW surface (as compared to the bulk) accounts for the majority of the ZPL shift. It should be pointed out that the magnitude of the ZPL shift and the relative importance of the four factors responsible for the ZPL tuning will change depending on a number of experimental details, including surface chemistries (different terminations, reconstructions, and chemical passivations [49,50]) and the implantation depth, as well as the sizes of the nanostructured crystals. Nonetheless, our results suggest a surprising approach to tuning defect emission frequencies using finite-size effects via shallow implantation of defects close to the surfaces and/or their placements in very small nanostructures.

V. CONCLUSIONS

In conclusion, our analysis shows that the spin state of V_{Si}^{-1} remains stable at different fourfold-coordinated defect sites in the NW, irrespective of the local strains. However, the optical properties of the quantum emitters show profound changes due to finite-size effects. Further, we find that the electronic, spin, and optical properties of the threefold sites are completely different, with the defects at these sites adopting a low-spin state. Also, due to considerable reconstruction around the undercoordinated defect sites and the fact that fewer covalent bonds need to be broken in creating the silicon vacancies, these sites have much lower defect-formation energies. These findings suggest that thermodynamically, the surfaces might act as a sink for the defects, with the defects at these sites no longer operating as bright defects. The kinetics of defect migration and the migration pathways to the surfaces of nanostructures are expected to depend on a number of factors, including nanostructure sizes, surface chemistries, and/or the presence of other intrinsic and extrinsic defects, and need to be explored in future studies. We also show that the photoexcitation process itself might result in deterioration of the signal from the defect due to the participation of the surface states. Such defects will be unusable for different applications designed around their spin state and our ability to control and manipulate these spins will be lost over time. This work is an important step toward understanding experiments and devising mitigating protocols that may include surface passivation and better positioning of the implanted defects. Study of the effects of surface chemistry on the properties of the defects and the kinetics of defect migration would be an exciting extension of this work. With a better understanding of the finite-size and surface effects, one can use nanostructuring as a tool to tune the optical properties of the defects themselves.

ACKNOWLEDGMENTS

We acknowledge support by the National Science Foundation (NSF) under NSF Grant No. DMR-1738076 and the Science and Technology Center (STC) for Integrated Quantum Materials under NSF Grant No. DMR-1231319. The computational support was provided by the Extreme Science and Engineering Discovery Environment (XSEDE) under Project PHY180014, which is supported by NSF Grant No. ACI-1548562. For three-dimensional visualization of crystals and volumetric data, the use of the VESTA 3 software is acknowledged.

P.D. conceived and directed the study. T.J. performed the ground-state calculations. P.D. performed the CDFT calculations and wrote the final manuscript, with inputs from the initial draft by T.J. Both authors proof read and reviewed the final revision of the manuscript.

[1] J. Weber, W. Koehl, J. Varley, A. Janotti, B. Buckley, C. Van de Walle, and D. Awschalom, Defects in SiC for quantum computing, J. Appl. Phys. **109**, 102417 (2011).

[2] S. G. Carter, O. O. Soykal, P. Dev, S. E. Economou, and E. R. Glaser, Spin coherence and echo modulation of the silicon vacancy in 4H-SiC at room temperature, Phys. Rev. B **92**, 161202 (2015).

[3] S. E. Economou and P. Dev, Spin-photon entanglement interfaces in silicon carbide defect centers, Nanotechnology **27**, 504001 (2016).

[4] R. Nagy, M. Widmann, M. Niethammer, D. B. Dasari, I. Gerhardt, Ö. O. Soykal, M. Radulaski, T. Ohshima, J. Vučković, and N. T. Son, *et al.*, Quantum Properties of

Dichroic Silicon Vacancies in Silicon Carbide, Phys. Rev. Appl. **9**, 034022 (2018).

[5] D. M. Lukin, C. Dory, M. A. Guidry, K. Y. Yang, S. D. Mishra, R. Trivedi, M. Radulaski, S. Sun, D. Vercruysse, and G. H. Ahn, *et al.*, 4H-silicon-carbide-on-insulator for integrated quantum and nonlinear photonics, Nat. Photonics **14**, 330 (2020).

[6] D. M. Lukin, A. D. White, R. Trivedi, M. A. Guidry, N. Morioka, C. Babin, Ö. O. Soykal, J. Ul-Hassan, N. T. Son, T. Ohshima, *et al.*, Spectrally reconfigurable quantum emitters enabled by optimized fast modulation, npj Quantum Inf. **6**, 1 (2020).

[7] M. Niethammer, M. Widmann, S.-Y. Lee, P. Stenberg, O. Kordina, T. Ohshima, N. T. Son, E. Janzén, and J. Wrachtrup, Vector Magnetometry Using Silicon Vacancies in 4 H-SiC Under Ambient Conditions, Phys. Rev. Appl. **6**, 034001 (2016).

[8] A. L. Falk, B. B. Buckley, G. Calusine, W. F. Koehl, V. V. Dobrovitski, A. Politi, C. A. Zorman, P. X.-L. Feng, and D. D. Awschalom, Polytype control of spin qubits in silicon carbide, Nat. Commun. **4**, 1 (2013).

[9] H. Seo, A. L. Falk, P. V. Klimov, K. C. Miao, G. Galli, and D. D. Awschalom, Quantum decoherence dynamics of divacancy spins in silicon carbide, Nat. Commun. **7**, 12935 (2016).

[10] R. Nagy, M. Niethammer, M. Widmann, Y.-C. Chen, P. Udvarhelyi, C. Bonato, J. U. Hassan, R. Karhu, I. G. Ivanov, N. T. Son, *et al.*, High-fidelity spin and optical control of single silicon-vacancy centres in silicon carbide, Nat. Commun. **10**, 1 (2019).

[11] D. J. Christle, A. L. Falk, P. Andrich, P. V. Klimov, J. U. Hassan, N. T. Son, E. Janzén, T. Ohshima, and D. D. Awschalom, Isolated electron spins in silicon carbide with millisecond coherence times, Nat. Mater. **14**, 160 (2015).

[12] F. Fuchs, B. Stender, M. Trupke, D. Simin, J. Pflaum, V. Dyakonov, and G. V. Astakhov, Engineering near-infrared single-photon emitters with optically active spins in ultrapure silicon carbide, Nat. Commun. **6**, 7578 (2015).

[13] J. Weber, W. Koehl, J. Varley, A. Janotti, B. Buckley, C. Van de Walle, and D. D. Awschalom, Quantum computing with defects, Proc. Natl. Acad. Sci. **107**, 8513 (2010).

[14] S. Castelletto and A. Boretti, Silicon carbide color centers for quantum application, J. Phys.: Photonics **2**, 022001 (2020).

[15] M. J. Polking, A. M. Dibos, N. P. de Leon, and H. Park, Improving defect-based quantum emitters in silicon carbide via inorganic passivation, Adv. Mater. **30**, 1704543 (2018).

[16] G. C. Vásquez, M. E. Bathen, A. Galeckas, C. Bazioti, K. M. Johansen, D. Maestre, A. Cremades, Ø. Prytz, A. M. Moe, A. Y. Kuznetsov, *et al.*, Strain modulation of Si vacancy emission from SiC micro- and nanoparticles, Nano Lett. **20**, 8689 (2020).

[17] M. N. Gadalla, A. S. Greenspon, R. K. Defo, X. Zhang, and E. L. Hu, Enhanced cavity coupling to silicon vacancies in 4H silicon carbide using laser irradiation and thermal annealing, Proc. Natl. Acad. Sci. **118**, e2021768118 (2021).

[18] S. Majety, V. A. Norman, L. Li, M. Bell, P. Saha, and M. Radulaski, Quantum photonics in triangular-cross-section nanodevices in silicon carbide, J. Phys.: Photonics **3**, 034008 (2021).

[19] A. L. Crook, C. P. Anderson, K. C. Miao, A. Bourassa, H. Lee, S. L. Bayliss, D. O. Bracher, X. Zhang, H. Abe, T. Ohshima, *et al.*, Purcell enhancement of a single silicon carbide color center with coherent spin control, Nano Lett. **20**, 3427 (2020).

[20] J. L. Zhang, S. Sun, M. J. Burek, C. Dory, Y.-K. Tzeng, K. A. Fischer, Y. Kelaita, K. G. Lagoudakis, M. Radulaski, Z.-X. Shen, *et al.*, Strongly cavity-enhanced spontaneous emission from silicon-vacancy centers in diamond, Nano Lett. **18**, 1360 (2018).

[21] D. O. Bracher, X. Zhang, and E. L. Hu, Selective Purcell enhancement of two closely linked zero-phonon transitions of a silicon carbide color center, Proc. Natl. Acad. Sci. **114**, 4060 (2017).

[22] M. Widmann, S.-Y. Lee, T. Rendler, N. T. Son, H. Fedder, S. Paik, L.-P. Yang, N. Zhao, S. Yang, I. Booker, *et al.*, Coherent control of single spins in silicon carbide at room temperature, Nat. Mater. **14**, 164 (2015).

[23] M. Radulaski, M. Widmann, M. Niethammer, J. L. Zhang, S.-Y. Lee, T. Rendler, K. G. Lagoudakis, N. T. Son, E. Janzen, T. Ohshima, *et al.*, Scalable quantum photonics with single color centers in silicon carbide, Nano Lett. **17**, 1782 (2017).

[24] Z. Yuan, M. Fitzpatrick, L. V. H. Rodgers, S. Sangtawesin, S. Srinivasan, and N. P. de Leon, Charge state dynamics and optically detected electron spin resonance contrast of shallow nitrogen-vacancy centers in diamond, Phys. Rev. Res. **2**, 033263 (2020).

[25] S. Sangtawesin, B. L. Dwyer, S. Srinivasan, J. J. Allred, L. V. Rodgers, K. De Greve, A. Stacey, N. Dontschuk, K. M. O'Donnell, D. Hu, *et al.*, Origins of Diamond Surface Noise Probed by Correlating Single-Spin Measurements with Surface Spectroscopy, Phys. Rev. X **9**, 031052 (2019).

[26] O. Soykal, P. Dev, and S. E. Economou, Silicon vacancy center in 4 H-SiC: Electronic structure and spin-photon interfaces, Phys. Rev. B **93**, 081207 (2016).

[27] P. Udvarhelyi, R. Nagy, F. Kaiser, S.-Y. Lee, J. Wrachtrup, and A. Gali, Spectrally Stable Defect Qubits with no Inversion Symmetry for Robust Spin-to-Photon Interface, Phys. Rev. Appl. **11**, 044022 (2019).

[28] C. Babin, R. Stöhr, N. Morioka, T. Linkewitz, T. Steidl, R. Wörnle, D. Liu, E. Hesselmeier, V. Vorobyov, A. Denisenko *et al.* Nanofabricated and integrated colour centres in silicon carbide with high-coherence spin-optical properties, ArXiv:2109.04737 (2021).

[29] J. Wang, X. Zhang, Y. Zhou, K. Li, Z. Wang, P. Peddibhotla, F. Liu, S. Bauerdick, A. Rudzinski, Z. Liu, *et al.*, Scalable fabrication of single silicon vacancy defect arrays in silicon carbide using focused ion beam, ACS Photonics **4**, 1054 (2017).

[30] S. P. Pavunny, A. L. Yeats, H. B. Banks, E. Bielejec, R. L. Myers-Ward, M. T. DeJarld, A. S. Bracker, D. K. Gaskill, and S. G. Carter, Arrays of Si vacancies in 4H-SiC produced by focused Li ion beam implantation, Sci. Rep. **11**, 3561 (2021).

[31] J. P. Perdew and W. Yue, Accurate and simple density functional for the electronic exchange energy: Generalized gradient approximation, Phys. Rev. B **33**, 8800 (1986).

[32] J. P. Perdew, K. Burke, and M. Ernzerhof, Generalized Gradient Approximation Made Simple, Phys. Rev. Lett. **77**, 3865 (1996).

[33] P. Giannozzi, S. Baroni, N. Bonini, M. Calandra, R. Car, C. Cavazzoni, D. Ceresoli, G. L. Chiarotti, M. Cococcioni, I. Dabo, *et al.*, QUANTUM ESPRESSO: A modular and open-source software project for quantum simulations of materials, J. Phys.: Condens. Matter **21**, 395502 (2009).

[34] P. Giannozzi, O. Andreussi, T. Brumme, O. Bunau, M. B. Nardelli, M. Calandra, R. Car, C. Cavazzoni, D. Ceresoli, M. Cococcioni, *et al.*, Advanced capabilities for materials modelling with QUANTUM ESPRESSO, J. Phys.: Condens. Matter **29**, 465901 (2017).

[35] H. J. Monkhorst and J. D. Pack, Special points for Brillouin-zone integrations, Phys. Rev. B **13**, 5188 (1976).

[36] A. Gali, E. Janzén, P. Deák, G. Kresse, and E. Kaxiras, Theory of Spin-Conserving Excitation of the N-V^- Center in Diamond, Phys. Rev. Lett. **103**, 186404 (2009).

[37] P. Dev, Fingerprinting quantum emitters in hexagonal boron nitride using strain, Phys. Rev. Res. **2**, 022050(R) (2020).

[38] P. Dev, Y. Xue, and P. Zhang, Defect-Induced Intrinsic Magnetism in Wide-Gap III Nitrides, Phys. Rev. Lett. **100**, 117204 (2008).

[39] P. Dev and P. Zhang, Unconventional magnetism in semiconductors: Role of localized acceptor states, Phys. Rev. B **81**, 085207 (2010).

[40] P. Dev, H. Zeng, and P. Zhang, Defect-induced magnetism in nitride and oxide nanowires: Surface effects and quantum confinement, Phys. Rev. B **82**, 165319 (2010).

[41] W. J. Huang, R. Sun, J. Tao, L. D. Menard, R. G. Nuzzo, and J. M. Zuo, Coordination-dependent surface atomic contraction in nanocrystals revealed by coherent diffraction, Nat. Mater. **7**, 308 (2008).

[42] See the Supplemental Material at http://link.aps.org/supplemental/10.1103/PRXQuantum.3.020325 for the electronic structure properties of the negatively-charged silicon vacancy at the threefold site on the NW surface, additional isosurface plots (smaller isovalue than the main text) for the defect states for a negatively-charged silicon vacancy in the NW interior, and the electronic structure properties of the neutral silicon vacancy in the 2H-SiC bulk and the NW.

[43] M. Kaviani, P. Deák, B. Aradi, T. Frauenheim, J.-P. Chou, and A. Gali, Proper surface termination for luminescent near-surface NV centers in diamond, Nano Lett. **14**, 4772 (2014).

[44] G. Wolfowicz, S. J. Whiteley, and D. D. Awschalom, Electrometry by optical charge conversion of deep defects in 4H-SiC, Proc. Natl. Acad. Sci. **115**, 7879 (2018).

[45] A. Zywietz, J. Furthmüller, and F. Bechstedt, Vacancies in SiC: Influence of Jahn-Teller distortions, spin effects, and crystal structure, Phys. Rev. B **59**, 15166 (1999).

[46] L. Torpo, R. M. Nieminen, K. E. Laasonen, and S. Pöykkö, Silicon vacancy in SiC: A high-spin state defect, Appl. Phys. Lett. **74**, 221 (1999).

[47] P. Deák, J. Miró, A. Gali, L. Udvardi, and H. Overhof, The spin state of the neutral silicon vacancy in 3C-SiC, Appl. Phys. Lett. **75**, 2103 (1999).

[48] D. A. Golter and C. W. Lai, Optical switching of defect charge states in 4H-SiC, Sci. Rep. **7**, 13406 (2017).

[49] R. Rurali, Electronic and structural properties of silicon carbide nanowires, Phys. Rev. B **71**, 205405 (2005).

[50] A. Miranda and L. Pérez, Electronic properties of fluorinated silicon carbide nanowires, Comput. Mater. Sci. **111**, 294 (2016).